ACS APPLIED MATERIALS & INTERFACES

Research Article

www.acsami.org

Facile Preparation of Hierarchical Structures Using Crystallization-Kinetics Driven Self-Assembly

Jinguang Cai,[†,‡] Chao Lv,[‡] and Akira Watanabe*[,†]

[†]Institute of Multidisciplinary Research for Advanced Materials, Tohoku University, 2-1-1 Katahira, Aoba-ku, Sendai 980-8577, Japan

[‡]China Academy of Engineering Physics, P.O. Box 919-71, Mianyang 621900, Sichuan, People's Republic of China

Supporting Information

ABSTRACT: Hierarchical structures (HSs) constructed by nanoparticle-based building blocks possess not only the properties of the primary building blocks but also collective properties of the assemblies. Here we report the facile preparation of hierarchical Ag nanoparticles/polyhedral oligomeric silsequioxane molecule (POSS) hybrid branched structures within tens of seconds by using spin-coating and doctor-blade methods. An assembly mechanism mainly controlled by POSS-crystallization kinetics and space resistance of Ag nanoparticles toward the diffusion of POSS molecules was tentatively proposed. It was demonstrated as a universal method for the preparation of hierarchical hybrid branched structures on arbitrary substrates, as well as by using other different POSS and inorganic nanoparticles. As a demonstration, Ag hierarchical structures obtained by heat treatment exhibit excellent SERS performance with enhancement factors as high as on the order of 10^7, making them promising sensors for the detection of trace amount of analyte adsorbed on the surface. Two-dimensional SERS mapping was also demonstrated by using a direct imaging system with high mapping speed and high resolution. Moreover, the substrates with Ag hierarchical structures were used as a SERS sensor for *in situ* detection due to the excellent SERS performance and stability of the structures.

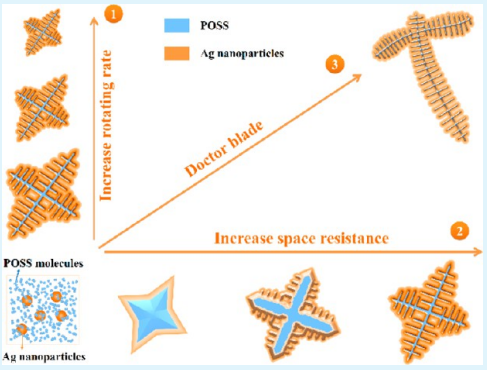

KEYWORDS: *hierarchical structures, hybrid materials, crystallization-driven self-assembly, POSS, SERS*

1. INTRODUCTION

Hierarchical structures (HSs) constructed by nanoparticle-based building blocks, which possess not only the properties of the primary building blocks but also collective properties of the assemblies, exhibit potential applications in various areas including life sciences, microelectronics, light manipulation, environment, and energy harvesting and storage.[1−7] Coassembly of different building blocks including inorganic nanoparticles and organic components via bottom-up methods has the potential to generate promising multifunctional hybrid composites combining the advantages of all of the element building blocks on the periodic table.[8] Therefore, it is important and challenging to develop facile effective and universal methods to fabricate hybrid HSs with controllable components and morphologies, as well as improved performance.

Recently, many approaches such as solvent mediated self-assembly of nanoparticles,[9,10] DNA or polymer-controlled organization of nanoparticles,[7,11−19] and pattern-modulated casting assembly of nanoparticles,[20−22] have been developed to construct HSs with different sizes and morphologies, as well as the interparticle space. During them, crystallization-driven self-assembly (CDSA) was developed as a particularly promising approach to fabricate well-defined HSs from block copolymers.[23−33] Generally, typical crystallized blocks, such as polyacrylonitrile (PAN),[34] polyethylene (PE),[35] poly(ethylene oxide),[36] poly(ferrocenyl dimethylsilane) (PFDMS),[37] poly(ε-caprolactone) (PCL),[38] poly(3-hexylthiophene) (P3HT),[25] or stereoregular polylactides (srPLA),[39] are necessary in the polymer chain to drive the crystallization process,[40] and other groups can be grafted on the crystallized cores to achieve higher level assembly and multifunctionality. However, most of these types of block polymers can only form one-dimensional cylindrical or wormlike crystalline-core micelles through the CDSA method.[40] A polyhedral oligomeric silsequioxane (POSS)-based hybrid polymer contains crystallizable hydrophobic POSS moieties, to which other various functional hydrophilic polymers or groups can be linked, thus resulting in abundant self-assembly behaviors in bulk, solution, and thin films, such as periodical nanostructures, microphase-separated nanostructures, spherical core−shell micelles, cylinders, vesicles, and thin films with ordered structures.[41−51] POSS-based molecules have been developed to prepare high-order structures via the CDSA mechanism. For example, recently, Yu et al. demonstrated the formation of square nanosheets with tunable size by living crystallization-driven 2D self-assembly of hyperbranched poly(ether amine) capped with heptaisobutyl-POSS.[40] However, most of the structures constructed by CDSA are soft matters, and it is still a big challenge to prepare hybrid

Received: June 11, 2015
Accepted: August 6, 2015
Published: August 6, 2015

DOI: 10.1021/acsami.5b05177
ACS Appl. Mater. Interfaces 2015, 7, 18697−18706

HSs through coassembly of inorganic nanoparticles and organic molecules by crystallization-driven self-assembly.

In this work, we demonstrate a facile universal approach for the preparation of hybrid HSs based on inorganic nanoparticles and POSS molecules through POSS-crystallization-kinetics driven self-assembly of nanoparticles during the process of solvent evaporation. By adjusting the octavinyl-POSS (OV-POSS) crystallization kinetic process, various HSs, such as size-controllable cross-star branches and long-band branches, are easily fabricated within tens of seconds. Actually, the branched HSs are three-level structures: the primary micrometer-scale cross-star or long-band branches, secondary submicrometer-scale sub-branches assembled by OV-POSS bones, and tertiary nanoscale inorganic nanoparticles. An assembly mechanism mainly controlled by POSS-crystallization kinetics and space resistance from inorganic nanoparticles against the diffusion of POSS molecules, is tentatively proposed. Moreover, this method and mechanism can be extended to other POSS molecules and inorganic nanoparticles, and similar hybrid HSs can also be easily fabricated on arbitrary substrates inclusive of flexible sheets. In addition, as a demonstration, the silver (Ag) HSs obtained after heat treatment of Ag/POSS hybrid HSs exhibit a high enhancement performance in the surface-enhanced Raman scattering (SERS) with an enhancement factor as high as on the order of 10^7. Two-dimensional (2D) SERS image is also obtained by a direct imaging system. Furthermore, the substrate with Ag HSs is demonstrated as an effective SERS sensor for *in situ* detection of chemical contaminants on a fruit peel.

2. EXPERIMENTAL SECTION

2.1. Materials and Preparation. The Ag, gold (Au), copper (Cu), and indium−tin (InSn) alloy nanoparticle inks were purchased from ULVAC Technologies Inc. Octavinyl-silsesquioxane (OV-POSS) and Octacyclohexyl-silsesquioxane (OCH-POSS) were purchased from Sigma-Aldrich. Toluene (99.8%) and *p*-aminothiophenol (PATP, 97%) were obtained from Wako Pure Chemical Industries. All of the chemicals were used as received.

Preparation of Inorganic Nanoparticles/POSS Hybrid Hierarchical Structures (HSs). Generally, hybrid HSs were prepared by spin-coating the mixed dispersion of inorganic nanoparticles and POSS molecules.[52] In a typical preparation, 20 μL of 25 wt % Ag nanoparticle dispersion in toluene was first mixed uniformly with 100 μL of 5 wt % of OV-POSS solution in toluene, and then the dispersion was spin-coated (MS-A100, Mikasa Co., Ltd.) on the glass substrates at room temperature in air at a rotating speed of 2000 rpm for 30 s with 5 s accelerating time from 0 to 2000 rpm. For the preparation of long-band branch HSs, the doctor-blade method was adopted by using a polyimide (PI) tape with a thickness of 50 μm on a substrate. Typically, the PI tape was first adhered to two opposite edges of a cleaned glass substrate, forming a groove with width of about 6 mm between these two tapes, and then 50 μL of the same mixed dispersion was dropped on one end of the groove. A glass rod was employed to scrape off the dispersion from the side with dispersion to the other empty side, leaving a thin layer dispersion with thickness of about 50 μm. The solvent in the remaining dispersion would be evaporated within several seconds, resulting in the long-band branched HSs. Without any other specifications, the total volume of the mixture dispersion was kept at 120 μL. After the preparation, POSS was removed by heat treatment on a hot plate at 250 °C for 30 min in air.

2.2. Characterization. The samples were characterized by optical microscopy (Olympus BX51), powder X-ray diffraction (XRD, Rigaku Smart Lab 9SW, Cu Kα radiation), scanning electron microscopy (SEM, Hitachi S4800, 10 kV), UV−vis absorption spectroscopy (JASCO V-670 spectrophotometer), and FT-IR spectroscopy (JASCO FT/IR-4200 spectrometer). The film thicknesses were observed by a color 3D laser microscope (KEYENCE VK-9700).

2.3. Raman Measurements. All the Raman spectra were acquired on a micro-Raman spectrometer equipped with an optical microscope (Olympus BX51), a 532 nm DPSS CW laser (MGL-H-532 nm-1 W, CNI), a CCD camera (DV401, Andor Technology), and a monochromator (MS257, Oriel Instruments Co.). The substrates with Ag HSs obtained after heat treatment were used for SERS measurements. For the preparation of SERS samples, the *p*-aminothiophenol (PATP) molecules were adsorbed on the surface of Ag HSs by immersing in 2 mM PATP solution in ethanol for 12 h to ensure a saturated coverage of PATP. After rinsed thoroughly with ethanol and dried in air, the SERS spectra of PATP were recorded. The detection limit was achieved by analyzing the SERS signals with different PATP concentrations. The reproducibility was demonstrated by recording SERS signals with at least 5 different points in one HS for above 6 HSs randomly selected on the substrate.

For the *in situ* Raman measurement on a fruit peel, a homemade sample holder was employed to fix an apple and a substrate with Ag HSs, which can be placed under an objective lens of Raman instrument (Figure S1). The apple bought from the market was first put in the bottom plate of the holder, and 20 μL of 1 mM PATP solution in ethanol was dropped on the apple skin as mimic contamination. The Raman signals of PATP molecules on the apple skin without Ag HSs were picked up as reference after evaporation of the solvent. The backside of the glass substrate with Ag HSs was pasted on the hole of the top plate of the sample holder using a double-side tape, and the glass substrate on top plate was tightly attached to the surface of the apple skin with PATP molecules with some pressure by tightening screws of the sample holder. The SERS signals were observed from the apple skin through the hole and the transparent glass substrate.

2.4. Two-Dimensional (2D) Raman Imaging. The 2D Raman imaging experiment was conducted on a homemade instrument. The 532 nm laser was introduced into the samples by a fiber, and the 2D Raman image of the sample was captured by using a low-temperature CCD camera (AP260EP, Apogee Imaging Systems) with a resolution of 512 px × 512 px and working temperature of −15 °C. A bandpass filter (FF01-579/34-25, center wavelength: 579 nm, >90% over 34 nm, Semrock, Inc.) was used to pass selectively through the SERS Raman bands in the region from 920 to 2150 cm^{-1}. The accumulating time was 60 s.

3. RESULTS AND DISCUSSION

3.1. Morphology and Structures. The typical chemicals employed in this work are octavinyl-POSS (OV-POSS) from Sigma-Aldrich, and uniform Ag nanoparticles with a size of about 4.5 nm dispersed in toluene from ULVAC Technologies Inc. OV-POSS can be easily crystallized from its toluene solution by evaporation, forming large crystals of parallelepiped shape with a specific angle around 96° (Figure S2a). The analysis of corresponding X-ray diffraction (XRD) spectrum shows that OV-POSS crystal belongs to a monoclinic crystal system with lattice parameters of a = 9.16 Å, b = 6.83 Å, c = 9.10 Å, α = 90°, β = 96.33°, and γ = 90° (Figure S2b,c). The preparation process of Ag/OV-POSS hybrid HSs by the spin-coating method is schematically illustrated in Figure 1a. For the typical sample, 20 μL of 25 wt % Ag nanoparticle dispersion in toluene was first thoroughly mixed with 100 μL of 5 wt % OV-POSS solution in toluene, and then spin-coated on clean glass substrates at 2000 rpm for 30 s with 5 s accelerating time. Before spin-coating, the mixed dispersion showed no precipitation. OV-POSS was removed by heat treatment on a hot plate at 250 °C for 30 min in air.[53]

Figure 1b shows a representative low-magnification optical microscopy (OM) image of the Ag/OV-POSS hybrid HSs formed on the substrate, suggesting the formation of cross-star structures with a scale of about 30−60 μm over a large area.

DOI: 10.1021/acsami.5b05177
ACS Appl. Mater. Interfaces 2015, 7, 18697−18706

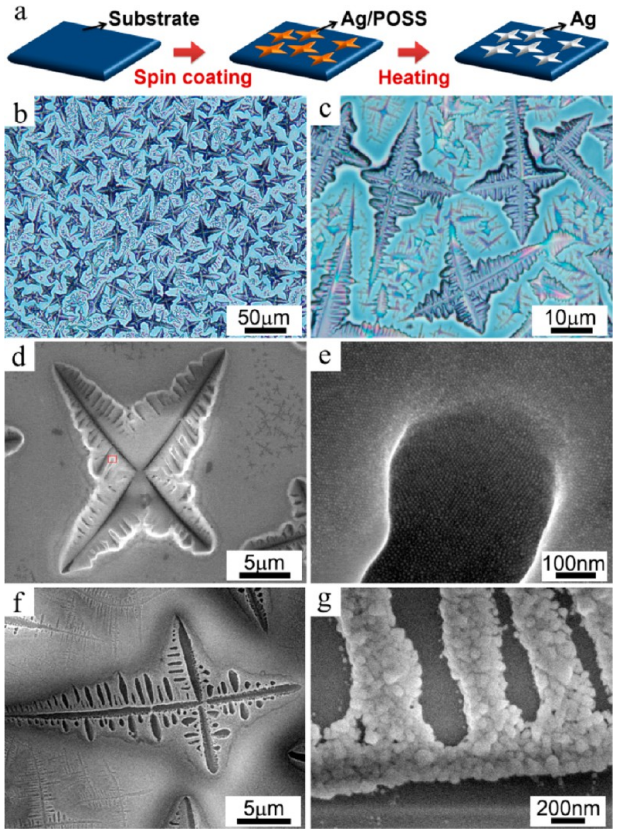

Figure 1. (a) Schematic diagram illustrating the preparation of Ag/OV-POSS hierarchical structures (HSs) and following evaporation of OV-POSS by heat treatment. Optical microscopy (OM) images (b, c), SEM image (d) and enlarged SEM image (e) of red rectangle area in (d) of Ag/OV-POSS hybrid HSs prepared by spin-coating at 2000 rpm for 30 s with 5 s accelerating time. (f, g) Corresponding SEM images after heat treatment at 250 °C for 30 min.

The structures maintain similar shape and morphology, although they are not so monodispersed. XRD spectrum of the cross-star structures shows a strong diffraction peak at 9.7° corresponding to the (001) plane of OV-POSS, and the diffraction peaks of Ag nanoparticles cannot appear because of the small size (Figure S3). The comparison among FT-IR spectra of Ag nanoparticles with surface protection, pure OV-POSS, and cross-star hybrid structures demonstrates that the cross-star structures are hybrid structures composed of both OV-POSS molecules and Ag nanoparticles (Figure S4). A high-magnification OM image in Figure 1c shows that each branch of the cross-star structures consists of some sub-branches with the same direction, and the length decreases gradually from cross center to tip. The angles between the two neighbor primary branches in the cross center are kept at about 96° for most cross-star HSs, just the similar value as the angle of the OV-POSS crystal particles (Figure S2a), indicating the formation of the hybrid structures related to the crystallization of OV-POSS. Interestingly, such fractal patterns with various degrees of self-similarity are frequently found in nature, such as ferns, leaves, and peacock feathers. According to the 3D topography obtained by the laser microscope, the thickness of larger-size HSs is about 0.9−1.2 μm (Figure S5). The scanning electron microscopy (SEM) image of one single cross-star structure in Figure 1d clearly shows the branched HSs, and the dark parts with branched structures in the core should be OV-POSS, which can be clearly seen in the high-magnification SEM image of the bottom-left branch (Figure S6a), whereas bright surfaces are ascribed to Ag nanoparticles. It could also be found that Ag nanoparticles exist not only in the gap between sub-branches but also on the surface of the sub-branch edges, even fully covering the smaller sub-branches. Interestingly, a close observation of the branched structure surface of the red rectangle area in Figure 1e shows that Ag nanoparticles are orderly and densely assembled, even on the surface with high curvature. It is noted that it is not empty in other flat parts without HSs but still a thin layer of remaining self-assembled Ag nanoparticles (Figure S6b). To elucidate the detail structures, we treated the substrates with cross-star hybrid HSs on a hot plate at 250 °C for 30 min in air to remove OV-POSS. Both XRD and FT-IR spectra suggest that there is no OV-POSS remaining after heat treatment (Figures S3, S4). The corresponding SEM image in Figure 1f clearly shows cross-star HSs are kept, whereas the inner cores are fully removed, suggesting the inner cores are formed by OV-POSS crystals and surrounded by Ag nanoparticles. An enlarged image in Figure

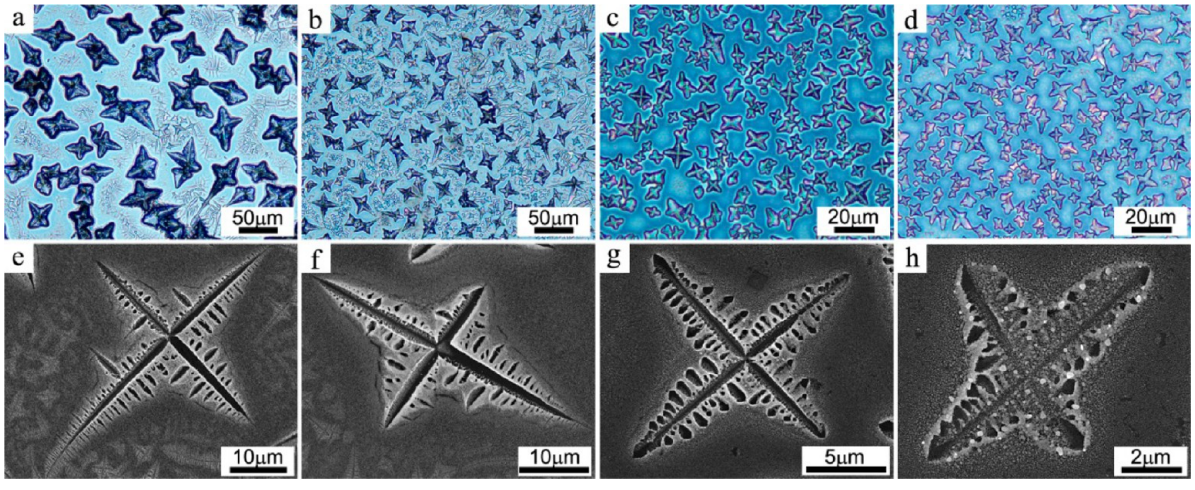

Figure 2. OM images (a−d) of Ag/OV-POSS hybrid HSs prepared by spin-coating at different rotating speeds without accelerating time, and corresponding SEM images (e−h) after heat treatment at 250 °C for 30 min in air. (a, e) 500 rpm, (b, f) 1000 rpm, (c, g) 2000 rpm, and (d, h) 3000 rpm.

DOI: 10.1021/acsami.5b05177
ACS Appl. Mater. Interfaces 2015, 7, 18697−18706

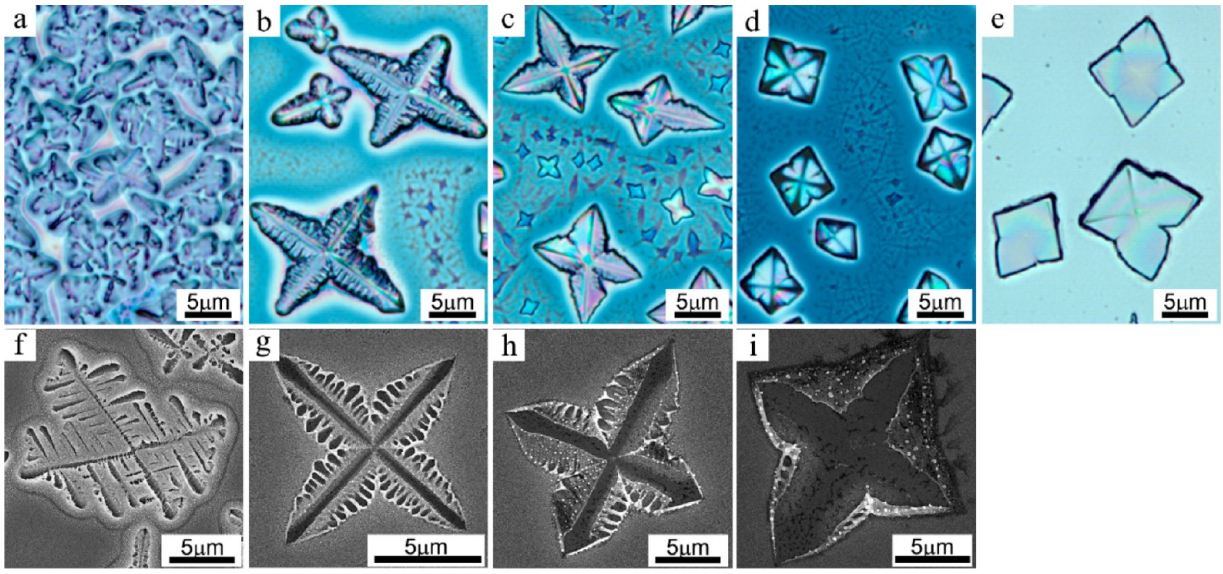

Figure 3. OM images of the as-prepared Ag/OV-POSS hybrid structures at the same OV-POSS concentration and different Ag concentrations (a–e), and SEM images of corresponding samples after heat treatment (f–i). Ag concentrations: (a, f) 62.5 wt %, (b, g) 12.5 wt %, (c, h) 6.25 wt %, (d, (i) 2.5 wt %, and (e) 0 wt %.

1g indicates the HSs comprise of Ag nanoparticles with size of several tens of nanometers, which is in accordance with the average crystallite size of about 25 nm from XRD pattern by calculating the peak of the Ag(111) reflection using the Scherrer equation (Figure S3). Separate Ag nanoparticles with similar size are also formed in the flat part of the substrates (Figure S6c). It suggests that the building block Ag nanoparticles of about 4.5 nm are fused into larger nanoparticles during the heat treatment process. Interestingly, the width of both OV-POSS branches and Ag branches of the HSs is located in hundred-nanometer scale, which means Ag nanoparticles can be assembled into ordered nanoscale HSs by this method. These results demonstrate that novel cross-star Ag/OV-POSS hybrid branched HSs with inner OV-POSS crystal cores, which possess three-level structures including primary micrometer-scale branches, secondary submicrometer-scale sub-branches assembled by OV-POSS bones, and tertiary nanoscale inorganic nanoparticles, are easily fabricated within tens of seconds by using a facile spin-coating method. In addition, hierarchical cross-star Ag branches consisting of Ag sub-branches assembled by interconnected larger Ag nanoparticles with average crystallite size of about 25 nm can also be easily obtained by simple heat treatment.

The spin-coating mode and rotating speed play a critical role in the formation of cross-star hybrid branched HSs. The typical sample is obtained by spin-coating at 2000 rpm for 30 s with 5 s accelerating time. Decreasing the rotating speed to 1000 rpm for 30 s with 5 s accelerating time or increasing the rotating speed to 3000 rpm for 30 s with 5 s accelerating time can produce similar cross-star hybrid branched HSs without obvious change of the size and morphology (Figure S7). It is because the 5 s accelerating time plays the critical role in the evaporation process, which is completed within 5–10 s. Therefore, to investigate the influence of rotating speeds on the HSs, we directly spin-coated the samples at different rotating speeds without accelerating time, and during this process the inherent accelerating time of the spin-coater is less than 1 s. The OM image of Ag/OV-POSS hybrid HSs prepared by spin-coating at 1000 rpm without accelerating time in Figure 2b and corresponding SEM image after heat treatment in Figure 2f exhibit the similar size and morphology as the typical sample prepared at 2000 rpm with a 5 s accelerating time. When the rotating speed rises to 2000 rpm without accelerating time, the size and thickness of the Ag/OV-POSS hybrid HSs are reduced to 10–25 μm and 500–800 nm, respectively (Figure 2c,g). Increasing the rotating speed to 3000 rpm without accelerating time leads to a further reduction of the structure size and thickness to about 5–15 μm and 300–500 nm (Figure 2d,f). If we decrease the rotating speed to 500 rpm without accelerating time, as shown in Figure 2a,e, the products are also cross-star branched HSs, and the size is not apparently changed, but the thickness is largely increased, to about 1.4–2 μm. Notably, all of these structures are hierarchical cross-star Ag/OV-POSS hybrid branched structures. However, if Ag/OV-POSS dispersion is directly drop-casted on the substrates without rotating, there are no Ag/OV-POSS hybrid cross-star branched HSs, and only the formation of large parallelepiped OV-POSS crystal particles with Ag nanoparticles surrounding is observed (Figure S8). Therefore, rotation is one of the key factors in the formation process of the cross-star Ag/OV-POSS hybrid branched HSs.

The concentrations of Ag nanoparticles and OV-POSS have a large influence on the formation of Ag/OV-POSS hybrid branched HSs. First, the effect of the concentration of original Ag nanoparticle dispersion was studied, while the OV-POSS concentration was kept constant at 5 wt %. When the concentration of the original Ag nanoparticle dispersion is increased from the typical 25 wt % to 62.5 wt %, hybrid branched HSs with longer branches are obtained, and the width of OV-POSS core branches becomes smaller (Figure 3a,f). If the concentration of Ag nanoparticle dispersion is decreased to 12.5 wt %, similar cross-star hybrid branched HSs as typical samples are obtained, whereas the size of POSS core crystal is increased a little bit (Figure 3b,g). If the concentration of Ag nanoparticle dispersion is reduced to 6.25 wt %, the structures changed largely. Though the structures maintain the cross-star morphology and the sub-branches remain, the OV-POSS cores become much larger (Figure 3c,h). When the concentration of

DOI: 10.1021/acsami.5b05177
ACS Appl. Mater. Interfaces 2015, 7, 18697–18706

Ag nanoparticles is further decreased to 2.5 wt %, the OV-POSS core becomes a large crystal, and the sub-branches almost disappear (Figure 3d,i). If only the OV-POSS solution is spin-coated, quasi-tetragon OV-POSS crystal particles are formed, without sub-branches (Figure 3e). Therefore, a relatively high concentration of Ag nanoparticles is one of the necessary parameters for the formation of branched HSs.

On the other hand, tuning the concentration of OV-POSS solution while keeping the concentration of Ag nanoparticle dispersion constant also influences the structures largely. When the concentration of OV-POSS solution is reduced to 2.5 wt % and the concentration of Ag nanoparticle dispersion was kept constant at 25 wt %, hybrid branched HSs are obtained with relatively longer branches and thinner thickness (Figure S9a,e). If the concentration of OV-POSS is decreased to 1.25%, there are no hierarchical branches formed, and only smaller cross-star OV-POSS cores without sub-branches are produced (Figure S9b,f). Further decrease of the OV-POSS concentration only results in small OV-POSS dots (Figure S9c,g). Ag nanoparticle dispersion without OV-POSS form uniform film assembled by Ag nanoparticles (Figure S9d,h). Therefore, an appropriate concentration of Ag nanoparticles is necessary for the formation of branched HSs.

A synchronous change of the concentrations of Ag nanoparticles and OV-POSS can also produce hybrid HSs with similar morphology but different size and thickness. For example, when both the concentrations of Ag nanoparticles and OV-POSS are reduced to half, i.e., 12.5 and 2.5 wt %, respectively, as shown in Figure S10, the products prepared by spin-coating at different rotating speeds also exhibit hybrid branched HSs. As the rotating speed increased, the sizes of the structures show a similar decrease tendency as that of typical concentrations. However, both the size and thickness are largely reduced (Table S1). Therefore, by tuning the rotating speeds and concentrations of Ag nanoparticles and OV-POSS, the size, thickness, and morphology of the Ag/OV-POSS hybrid HSs can be easily controlled.

Besides the spin-coating method, the doctor-blade method can also be employed to fabricate Ag/OV-POSS hybrid HSs. As shown in Figure 4a, uniform long band-like structures with length of tens of micrometers and thickness of 200−400 nm,

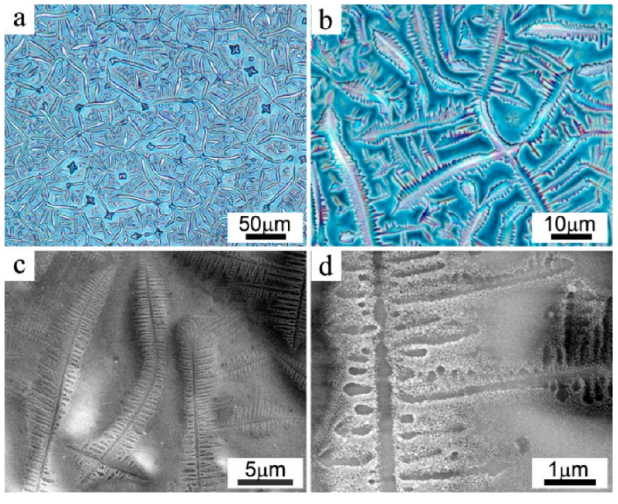

Figure 4. OM images (a, b) of Ag/OV-POSS composites prepared by a doctor-blading method, and corresponding SEM images (c, d) after heat treatment.

are produced, in spite of some occasional smaller cross-star structures. The enlarged OM image in Figure 4b shows the long band-like structures consist of sub-branches, even some sub-branches have secondary sub-branches, suggesting the formation of long-band branched HSs with self-similarity. After heat treatment, cores of the branched HSs become blank surrounded by remaining fused Ag nanoparticles (Figure 4c,d), indicating the long-band branched HSs are the similar structures as the typical samples obtained by the spin-coating method, consisting of OV-POSS core branches and surrounding Ag nanoparticles. Therefore, long-band Ag/OV-POSS hybrid HSs with OV-POSS cores consisting of submicrometer-scale sub-branches assembled by OV-POSS bones and nanoscale Ag nanoparticles are prepared by using a facile doctor-blade method. It may be noted that Lu et al. have reported similar fernlike Au nanoparticle/thiol-functionalized isobutyl-POSS (SH-POSS) hybrid micropatterns by drop-casting the SH-POSS protected Au nanoparticle dispersion.[54] However, the formation mechanism was different. The formation of Au/SH-POSS fernlike micropatterns was a thermodynamically controlled process, during which the excess of SH-POSS molecules crystallized into fernlike micropatterns, and then Au nanoparticles deposited onto the surface and interstices.

3.2. Formation Mechanism. On the basis of the above investigation, we propose a tentative formation mechanism of the Ag/OV-POSS hybrid branched HSs (Figure 5). When Ag

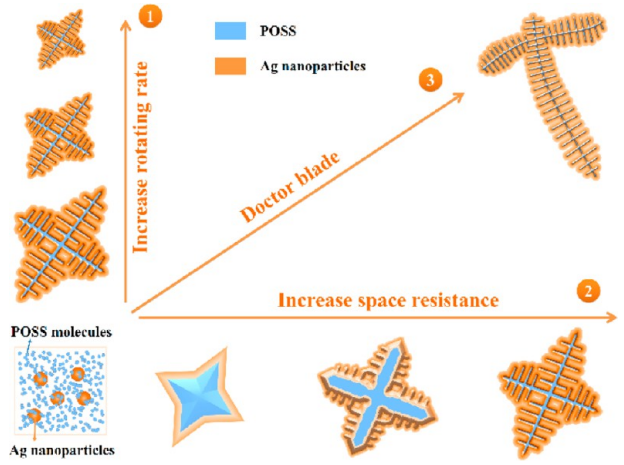

Figure 5. Schematic illustration of the formation mechanism of Ag/OV-POSS HSs controlled by crystallization-kinetics and space resistance.

nanoparticles and OV-POSS dispersion are drop-casted on the substrates, the solvent evaporation requires a long time, which is enough for the diffusion and crystallization of OV-POSS molecules to form large specific-shape crystals. When the mixture is spin-coated at a high rotating speed, there will be only a very thin film of dispersion remaining on the substrates, and the evaporation process is completed within only several seconds. During the very short period, OV-POSS molecules cannot diffuse freely to crystallize into a large crystal because of the space resistance from Ag nanoparticles. At the same time, OV-POSS molecules have preferential crystallization direction and a relatively uniform evaporation rate at each direction in the plane, thus forming hierarchical cross-star hybrid branch structures with a specific angle of about 96°. As the rotating speed increases, the remaining dispersion film becomes thinner,

DOI: 10.1021/acsami.5b05177
ACS Appl. Mater. Interfaces 2015, 7, 18697−18706

and the solvent evaporation time becomes shorter, thus inducing a faster crystallization process, and resulting in the formation of thinner and smaller cross-star branched HSs (Path 1 in Figure 5). On the other hand, as the concentration of Ag nanoparticles decreases, the resistance for OV-POSS molecule diffusion becomes weaker, and OV-POSS cores of the obtained structures grow larger and sub-branches gradually disappears (Path 2 in Figure 5). So, the space resistance from Ag nanoparticles against OV-POSS molecular diffusion is necessary for the formation of branched HSs. Therefore, fast evaporation and space resistance are two key factors for the formation of branched HSs. The long-band branched HSs fabricated by the doctor-blade method also demonstrate this mechanism. The thin dispersion film formed by the doctor-blade method also induces a fast solvent evaporation and fast crystallization of OV-POSS, and at the same time Ag nanoparticles act as obstructions to hinder the diffusion of OV-POSS molecules. However, this process is a little different from that of the spin-coating method. Instead of the uniform fast evaporation rate at each direction in the plane provided by the spin-coating method, the evaporation of the solvent from the thin layer dispersion made by the doctor-blade method lasts a little long time and the evaporation direction of the thin layer is not uniform but arbitrary, so long-band hybrid branched HSs with arbitrary directions instead of cross-star branched HSs are formed (Path 3 in Figure 5). Therefore, the formation of hybrid HSs is a fast solvent evaporation induced OV-POSS molecules diffusion-controlled crystallization-kinetics driven self-assembly process. In the heat treatment process, several neighboring Ag nanoparticle of 4.5 nm may be fused together with random crystal orientation, forming larger Ag nanoparticles with average crystallite size of about 25 nm. At the same time, with the sublimation of OV-POSS cores, Ag nanoparticles on the surface of OV-POSS cores may move to the edge, and be fused and dewetted during the fusion process, leaving relatively large empty places compared to exposed OV-POSS area in the hybrid structures.

3.3. Universal Method. It is noteworthy that the preparation of hybrid HSs via crystallization-kinetics driven self-assembly is a universal method. When OV-POSS solution is mixed with other inorganic nanoparticle dispersions with a suitable concentration, similar nanoparticles/OV-POSS hybrid branched HSs can be prepared. For example, Au/OV-POSS hybrid branched HSs with a size of 10−20 μm are fabricated by spin-coating the mixture of 20 μL of 30 wt % Au nanoparticle dispersion and 100 μL of 5 wt % OV-POSS solution (Figure 6a,b), and Cu/OV-POSS hybrid branched HSs with relatively longer sub-branches are formed by spin-coating the mixture of 20 μL of 15 wt % Cu nanoparticle dispersion and 100 μL of 5 wt % OV-POSS solution (Figure 6c,d). InSn alloy nanoparticles and OV-POSS dispersion can also form similar hybrid branched HSs by using the same spin-coating method (Figure 6e,f). This method can also be extended to other POSS molecules. For example, by using the spin-coating method, octacyclohexyl-POSS (OCH-POSS) and Ag nanoparticles can form similar cross-star Ag/OCH-POSS hybrid branched HSs with size of 10−20 μm, which comprise relatively longer sub-branches (Figure S11). Moreover, similar Ag/OV-POSS hybrid branched HSs can be fabricated on arbitrary substrates, such as silicon wafer, Al foil, Cu foil, hydrophobic polytetrafluoroethylene (PTFE), and even thin flexible polyimide (PI) film (Figure S12). Therefore, this crystallization-kinetics driven self-assembly is a universal method for the preparation of hybrid HSs of different nanoparticles and different POSS molecules on arbitrary substrates.

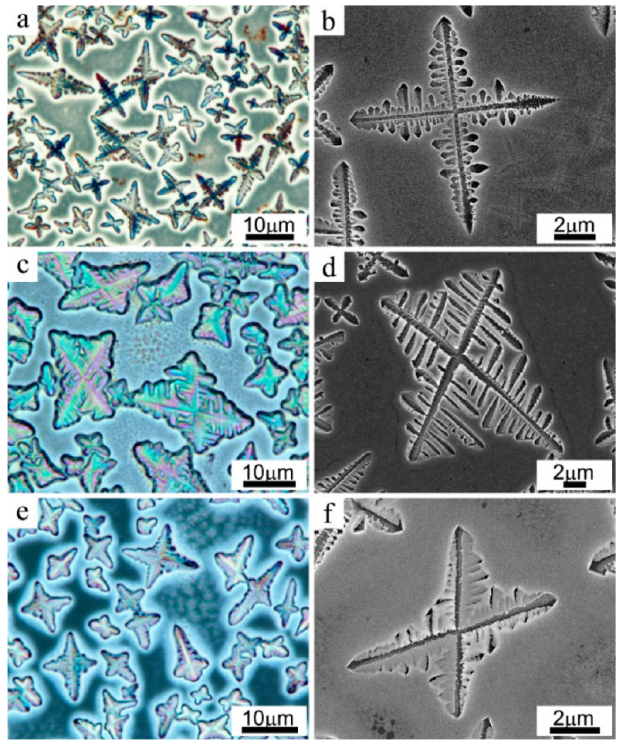

Figure 6. (a, c, e) OM images of different inorganic nanoparticles and OV-POSS composites obtained by spin-coating method, and corresponding SEM images after heat treatment (b, d, f). (a, b) Au, (c, d) Cu, and (e, f) InSn.

3.4. Optical Property. The corresponding UV−vis absorption spectra of the Ag nanoparticles/OV-POSS hybrid structures prepared at different OV-POSS concentrations without heat treatment are measured (Figure S13). As OV-POSS concentration increases, the absorption peak of characteristic surface plasmonic resonance (SPR) band of Ag nanoparticles is red-shifted from 455 nm for pure Ag nanoparticles to 472 nm for 5 wt % POSS concentration sample, accompanying the band broadening. The red shift of the SPR band may be derived from three main reasons, i.e., dielectric constant change in the surrounding of Ag nanoparticles caused by OV-POSS, Ag nanoparticles assembled following the OV-POSS crystal branches, and light scattering of the HSs. As shown in the absorption spectra, the red shift of SPR peaks may fall into two groups, one group with small red shift of 3 and 4 nm for 0.5 and 1.25 wt % OV-POSS samples, respectively, and the other group with a relatively large red shift of 12 and 17 nm for 2.5 and 5 wt % samples, respectively. For the first group, the small red shift may be due to the surrounding dielectric constant change of Ag nanoparticles. The dielectric constants of glass, OV-POSS, and air are about 3.8, 2.2, and 1, respectively. As the concentration of OV-POSS increased from 0 to 1.25%, the surrounding of Ag nanoparticles is partly replaced by OV-POSS instead of air and glass, and the increase of the average dielectric constant around Ag nanoparticles is not so apparent. At the same time, there are no branched HSs formed and no apparent assembly of Ag nanoparticles. So, the SPR peak of Ag nanoparticles is only slightly changed due to the minor increase of surrounding dielectric constant.[55,56] On the other hand, when the

DOI: 10.1021/acsami.5b05177
ACS Appl. Mater. Interfaces 2015, 7, 18697−18706

concentration of OV-POSS increased to more than 2.5 wt %, all of the three factors may have contributions to the red shift and broadening of the SPR peak. The increase of OV-POSS concentration would further increase the surrounding dielectric constant, inducing further red shift of the SPR peak. The assembly of Ag nanoparticles along the OV-POSS branches of the formed HSs which are thicker than flat Ag nanoparticle layers may also make the SPR peak red shift, and the nonuniformity of the assembly thickness may also broaden the SPR peak.[56] In addition, the sub-branches of HSs are almost located in the submicrometer scale, which would cause strong light scattering in the visible and infrared region, thus broadening the SPR peak with a long tail. Therefore, the optical property of the hierarchical hybrid structures can be easily varied by changing OV-POSS concentration.

3.5. SERS Performance. Hierarchical structures have potential applications in many areas, including life sciences, microelectronics, light manipulation, environment, and energy harvesting and storage. In this work, considering that Ag branched HSs obtained by heat treatment of hybrid HSs are composed of interconnected Ag nanoparticles, and have no surface capping agents, it is reasonably expected that the obtained Ag HSs could act as effective SERS substrates for the detection of trace amounts of molecules adsorbed on the surface. Although Ag nanoparticles/OV-POSS hybrid HSs also show enhanced Raman signals, here we only study the SERS performance of pure Ag HSs obtained after heat treatment, because Ag/OV-POSS hybrid HSs are not as stable as Ag HSs in mechanics and under laser irradiation and OV-POSS molecules inside are recognized as impurities for SERS measurement. The SERS signals of *p*-aminothiophenol (PATP) molecules adsorbed on the Ag HSs by Ag−S bonds were measured and the Raman signals of solid PATP and PATP molecules adsorbed on the Ag nanoparticle film obtained by heat-treating pure Ag nanoparticle films were also taken for comparison. As shown in Figure 7, compared with the Raman spectrum of solid PATP, remarkable changes in the Raman shift and relative intensity of the bands can be observed from the SERS spectra of the Ag HSs. The Raman scattering peaks located at 1016, 1083, 1196, and 1582 cm^{-1} corresponded to the a_1 vibration mode, whereas other peaks at 1152, 1397, and 1444 cm^{-1} corresponded to the b_2 vibration mode.[57−59] The Ag branched HSs showed relatively uniform excellent SERS performance for each of the primary branches (Lines 2−4 in Figure 7) and cross center (Line 1 in Figure 7), with much higher scattering intensity than the flat part with Ag nanoparticles instead of Ag HSs (Line 6 in Figure 7) and heat-treated pure Ag nanoparticle film (Control line in Figure 7). Generally, there are two mechanisms for the enhancement of PATP Raman signals: electromagnetic (EM) model and charge transfer (CT) model. The EM model is resulted from strong local enhancement of the electric field near the nanoparticles, with no requirement for specific bonds between adsorbates and metals, whereas the CT model needs direct proximity between the molecules and the surface for the transfer of charges from metal to molecules.[59] In this work, the enhancement of a_1 vibration by Ag HSs can be ascribed to the EM model, because the CT model almost has no effects for a_1 vibration enhancement.[59] The EM model may also have the same contribution to the b_2 vibration enhancement, but from the spectra it can be found that compared to a_1 vibration mode, the enhancement of b_2 vibration mode was relatively large, which may be derived from the charge transfer from Ag nanoparticles to the adsorbed PATP molecules.[58,59]

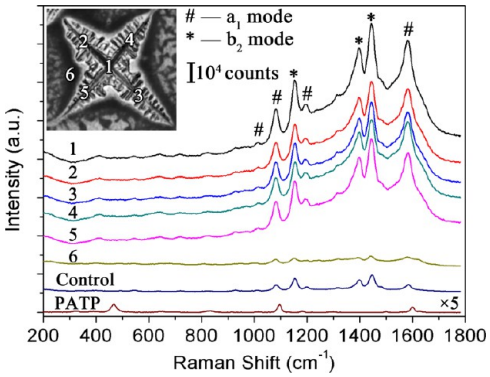

Figure 7. Raman spectrum of solid PATP, SERS spectrum of PATP molecules adsorbed on pure Ag nanoparticle film after heat treatment (Control line), and SERS spectra of PATP molecules at different parts of the substrates with Ag branched HSs obtained by heat-treating the typical Ag/OV-POSS hybrid HSs (1−6). Inset is corresponding single Ag branched HS in SERS measurement.

The enhancement factors (EF) of Ag HSs can be calculated by using the following equation:

$$EF = \frac{N_{bulk} I_{surf}}{N_{surf} I_{bulk}}$$

where N_{bulk} and N_{surf} represent the number of PATP molecules in the bulk solid sample and on the surface of Ag HSs, respectively; and I_{bulk} and I_{surf} are the Raman scattering intensities from the solid PATP and the PATP molecules adsorbed on the surface. On the basis of the measured values in Figure S14, the calculated EF values for the Ag HSs at two typical Raman shift peaks 1582 and 1444 cm^{-1}, which belong to the a_1 vibration mode and b_2 vibration mode, respectively, were 4.11×10^6 and 2.59×10^7. The high EF values could be attributed to the coupling of SPR between the neighboring branches and the internanoparticle "hot spots", which may be favorable for the detection of certain analyte at ultralow concentration. As a demonstration, after immersing the substrate with Ag HSs in 1 nM PATP solution, the substrate shows noticeable SERS signals of PATP molecules (Figure S15).

To elucidate intuitively the relative SERS performance of different parts on the substrate with Ag HSs, we studied two-dimensional (2D) SERS mapping via a new approach, in which a 2D SERS image is directly captured by combination of a high sensitive CCD camera and a bandpass filter with Raman bands passing through the region from 920 to 2150 cm^{-1}. In this approach, all of the passing-through signals are captured under control of the bandpass filter, quite different from the general scanning method, which measures all the Raman spectra point by point, and then the intensity at specific Raman peak is extracted to produce the 2D Raman image. In comparison, both methods have their advantages. With the point-by-point scanning method, the details of Raman signals at each Raman shift position can be obtained, and easily transferred to 2D Raman images at the specific Raman shift, but it is time-consuming, especially for high resolution and large-scale 2D images. With the CCD camera method, 2D Raman images can be obtained within tens of seconds, and the resolution and scale can be easily controlled by the lens of the optical microscopy,

DOI: 10.1021/acsami.5b05177
ACS Appl. Mater. Interfaces 2015, 7, 18697−18706

but only a 2D SERS image of specific Raman shift range controlled by the filter can be obtained. The OM image and corresponding as-captured 2D SERS image of PATP molecules absorbed on Ag HSs obtained after heat treatment are shown in Figure 8, which clearly indicates the Ag HSs exhibit relatively

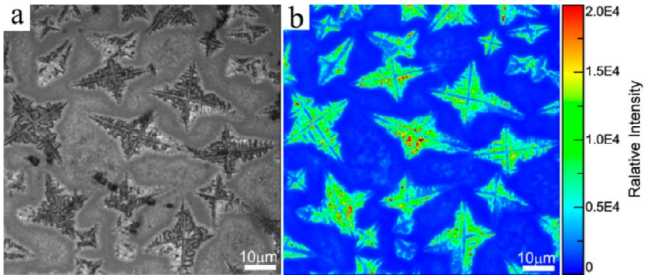

Figure 8. (a) Optical image and (b) SERS image of the PATP-adsorbed Ag HSs.

uniform and highest SERS intensity, especially the parts near the main branches. However, other flat parts that are only consisting of Ag nanoparticles other than Ag HSs exhibit much lower SERS intensity than that of Ag HSs parts. The results here are consistent with SERS spectra at different parts on the substrates in Figure 7, which demonstrate the SERS signals from the HSs are much higher than that from flat parts. It is worth mentioning, in spite of the small size in submicrometer scale, the SERS signals for the blank places formed inside the HSs after evaporation of OV-POSS can also be recorded by the CCD camera, which means that the CCD camera method has a high resolution for 2D Raman imaging.

Because Ag HSs show excellent SERS performance and can be fabricated on arbitrary substrates, the substrate with Ag HSs can be reasonably expected as an *in situ* SERS sensor. Before the measurement, the mechanical property of the Ag HSs on the glass substrate was tested. A Scotch tape was employed to peel off the Ag HSs, and no Ag HSs were peeled off from the substrate, with only some glue left from tape, suggesting an effective adhesion of the Ag HSs (Figure S16). For the *in situ* SERS measurement, PATP was adopted as mimic contamination and drop-casted on the apple skin, and Raman signals were measured with and without contact to the substrate with Ag HSs (for operations, see the Experimental Section and Figure S1). As shown in Figure 9, there were no apparent Raman signals from the apple skin before the substrate contacted, but SERS signals were largely enhanced after the

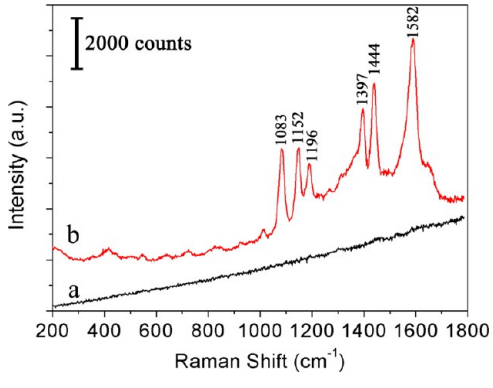

Figure 9. Raman spectra of PATP molecules casted on the apple skin before (a) and after Ag HSs contacted (b).

substrate contacted with similar Raman shift peaks as the result in Figure 7, which can be ascribed to the excellent SERS performance of the Ag HSs on the substrate. After measurements, the substrate with Ag HSs showed no obvious change of Ag hierarchical structures (Figure S17), demonstrating its high mechanical stability, in accordance with the result of tape-peeling experiment. Therefore, it is expected the substrate with Ag HSs can act as an effective SERS sensor for *in situ* detection of contamination, pesticide, and biomolecules.

4. CONCLUSIONS

We achieved the facile preparation of unique Ag/POSS hybrid HSs by a spin-coating or doctor-blade method, which can be completed within tens of seconds. The size, thickness, and morphology can be easily controlled by adjusting rotating speeds and concentrations. A tentative mechanism of crystallization-kinetics driven self-assembly during the evaporation process was proposed, which is demonstrated as a universal method for the preparation of hybrid branched HSs on arbitrary substrates, as well as by using other different POSS and nanoparticles. As a demonstration, Ag HSs obtained by heat treatment exhibit excellent SERS performance with enhancement factors as high as on the order of 10^7 and a low detection limit of 1 nM, making them promising sensors for the detection of trace amount of analyte adsorbed on the surface. Two-dimensional (2D) SERS mapping by a direct imaging system was also demonstrated. Furthermore, as expected, the substrates with Ag HSs can act as a SERS sensor for *in situ* detection due to the excellent SERS performance and stability of the structures. This work paves the way to fabricate various novel hybrid HSs via the crystallization-kinetics driven self-assembly method, which has potential to be extended to other building blocks and crystals, such as semiconductor nanoparticles and inorganic salts with different crystal forms.

■ ASSOCIATED CONTENT

Supporting Information

The Supporting Information is available free of charge on the ACS Publications website at DOI: 10.1021/acsami.5b05177.

XRD patterns, FT-IR spectra, UV−vis absorption spectra, Raman spectra, 3D topographic image, digital and OM images (PDF).

■ AUTHOR INFORMATION

Corresponding Author

*A. Watanabe. E-mail: watanabe@tagen.tohoku.ac.jp. Fax: (+81) 22 217 5851. Phone: (+81) 22 217 5851.

Author Contributions

The paper was written through contributions of all authors. All authors have given approval to the final version of the paper.

Notes

The authors declare no competing financial interest.

■ ACKNOWLEDGMENTS

This work was supported by MEXT KAKENHI Grant Number 24102004 and JSPS KAKENHI Grant Number 15H04132, China Academy of Engineering Physics (item no. TP201302-3), and the Fundamental Application Research of the Department of Science and Technology of Sichuan Province (grant no. 2014JY0137). The authors thank Professor Tienan

DOI: 10.1021/acsami.5b05177
ACS Appl. Mater. Interfaces 2015, 7, 18697−18706

Jin for the help of XRD measurement at the Center for Integrated Nanotechnology Support, Tohoku University.

REFERENCES

(1) Ye, J.; Liu, W.; Cai, J.; Chen, S.; Zhao, X.; Zhou, H.; Qi, L. Nanoporous Anatase TiO_2 Mesocrystals: Additive-Free Synthesis, Remarkable Crystalline-Phase Stability, and Improved Lithium Insertion Behavior. *J. Am. Chem. Soc.* **2011**, *133*, 933−940.
(2) Nie, Z.; Petukhova, A.; Kumacheva, E. Properties and Emerging Applications of Self-Assembled Structures Made from Inorganic Nanoparticles. *Nat. Nanotechnol.* **2010**, *5*, 15−25.
(3) Talapin, D. V.; Lee, J.-S.; Kovalenko, M. V.; Shevchenko, E. V. Prospects of Colloidal Nanocrystals for Electronic and Optoelectronic Applications. *Chem. Rev.* **2010**, *110*, 389−458.
(4) Cai, J.; Ye, J.; Chen, S.; Zhao, X.; Zhang, D.; Chen, S.; Ma, Y.; Jin, S.; Qi, L. Self-Cleaning, Broadband and Quasi-Omnidirectional Antireflective Structures Based on Mesocrystalline Rutile TiO_2 Nanorod Arrays. *Energy Environ. Sci.* **2012**, *5*, 7575−7581.
(5) Talapin, D. V.; Murray, C. B. PbSe Nanocrystal Solids for n- and p-Channel Thin Film Field-Effect Transistors. *Science* **2005**, *310*, 86−89.
(6) Huynh, W. U.; Dittmer, J. J.; Alivisatos, A. P. Hybrid Nanorod-Polymer Solar Cells. *Science* **2002**, *295*, 2425−2427.
(7) Lopes, W. A.; Jaeger, H. M. Hierarchical Self-Assembly of Metal Nanostructures on Diblock Copolymer Scaffolds. *Nature* **2001**, *414*, 735−738.
(8) Balazs, A. C.; Emrick, T.; Russell, T. P. Nanoparticle Polymer Composites: Where Two Small Worlds Meet. *Science* **2006**, *314*, 1107−1110.
(9) Xiao, J.; Li, Z.; Ye, X.; Ma, Y.; Qi, L. Self-Assembly of Gold Nanorods into Vertically Aligned, Rectangular Microplates with a Supercrystalline Structure. *Nanoscale* **2014**, *6*, 996−1004.
(10) Quan, Z.; Xu, H.; Wang, C.; Wen, X.; Wang, Y.; Zhu, J.; Li, R.; Sheehan, C. J.; Wang, Z.; Smilgies, D.-M.; Luo, Z.; Fang, J. Solvent-Mediated Self-Assembly of Nanocube Superlattices. *J. Am. Chem. Soc.* **2014**, *136*, 1352−1359.
(11) Deng, Z. X.; Tian, Y.; Lee, S. H.; Ribbe, A. E.; Mao, C. D. DNA-Encoded Self-Assembly of Gold Nanoparticles into One-Dimensional Arrays. *Angew. Chem., Int. Ed.* **2005**, *44*, 3582−3585.
(12) Wang, Z. G.; Ding, B. Q. DNA-Based Self-Assembly for Functional Nanomaterials. *Adv. Mater.* **2013**, *25*, 3905−3914.
(13) Wang, Z.-G.; Ding, B. Engineering DNA Self-Assemblies as Templates for Functional Nanostructures. *Acc. Chem. Res.* **2014**, *47*, 1654−1662.
(14) Bockstaller, M. R.; Mickiewicz, R. A.; Thomas, E. L. Block Copolymer Nanocomposites: Perspectives for Tailored Functional Materials. *Adv. Mater.* **2005**, *17*, 1331−1349.
(15) Akcora, P.; Liu, H.; Kumar, S. K.; Moll, J.; Li, Y.; Benicewicz, B. C.; Schadler, L. S.; Acehan, D.; Panagiotopoulos, A. Z.; Pryamitsyn, V.; Ganesan, V.; Ilavsky, J.; Thiyagarajan, P.; Colby, R. H.; Douglas, J. F. Anisotropic Self-Assembly of Spherical Polymer-Grafted Nanoparticles. *Nat. Mater.* **2009**, *8*, 354−359.
(16) Dey, P.; Blakey, I.; Thurecht, K. J.; Fredericks, P. M. Hyperbranched Polymer−Gold Nanoparticle Assemblies: Role of Polymer Architecture in Hybrid Assembly Formation and SERS Activity. *Langmuir* **2014**, *30*, 2249−2258.
(17) Mezour, M. A.; Perepichka, I. I.; Zhu, J.; Lennox, R. B.; Perepichka, D. F. Directing the Assembly of Gold Nanoparticles with Two-Dimensional Molecular Networks. *ACS Nano* **2014**, *8*, 2214−2222.
(18) Ku, K. H.; Shin, J. M.; Kim, M. P.; Lee, C.-H.; Seo, M.-K.; Yi, G.-R.; Jang, S. G.; Kim, B. J. Size-Controlled Nanoparticle-Guided Assembly of Block Copolymers for Convex Lens-Shaped Particles. *J. Am. Chem. Soc.* **2014**, *136*, 9982−9989.
(19) Kao, J.; Thorkelsson, K.; Bai, P.; Zhang, Z.; Sun, C.; Xu, T. Rapid Fabrication of Hierarchically Structured Supramolecular Nanocomposite Thin Films in One Minute. *Nat. Commun.* **2014**, *5*, 4053.
(20) Hanske, C.; Tebbe, M.; Kuttner, C.; Bieber, V.; Tsukruk, V. V.; Chanana, M.; König, T. A. F.; Fery, A. Strongly Coupled Plasmonic Modes on Macroscopic Areas via Template−Assisted Colloidal Self-Assembly. *Nano Lett.* **2014**, *14*, 6863−6871.
(21) Asbahi, M.; Mehraeen, S.; Lim, K. T. P.; Wang, F.; Cao, J.; Tan, M. C.; Yang, J. K. W. Template-Induced Structure Transition in Sub-10nm Self-Assembling Nanoparticles. *Nano Lett.* **2014**, *14*, 2642−2646.
(22) Hamon, C.; Novikov, S.; Scarabelli, L.; Basabe-Desmonts, L.; Liz-Marzán, L. M. Hierarchical Self-Assembly of Gold Nanoparticles into Patterned Plasmonic Nanostructures. *ACS Nano* **2014**, *8*, 10694−10703.
(23) Wang, X.; Guerin, G.; Wang, H.; Wang, Y.; Manners, I.; Winnik, M. A. Cylindrical Block Copolymer Micelles and Co-Micelles of Controlled Length and Architecture. *Science* **2007**, *317*, 644−647.
(24) Gilroy, J. B.; Gädt, T.; Whittell, G. R.; Chabanne, L.; Mitchels, J. M.; Richardson, R. M.; Winnik, M. A.; Manners, I. Monodisperse Cylindrical Micelles by Crystallization-Driven Living Self-Assembly. *Nat. Chem.* **2010**, *2*, 566−570.
(25) Patra, S. K.; Ahmed, R.; Whittell, G. R.; Lunn, D. J.; Dunphy, E. L.; Winnik, M. A.; Manners, I. Cylindrical Micelles of Controlled Length with a π-Conjugated Polythiophene Core via Crystallization-Driven Self-Assembly. *J. Am. Chem. Soc.* **2011**, *133*, 8842−8845.
(26) Gröschel, A. H.; Schacher, F. H.; Schmalz, H.; Borisov, O. V.; Zhulina, E. B.; Walther, A.; Müller, A. H. E. Precise Hierarchical Self-Assembly of Multicompartment Micelles. *Nat. Commun.* **2012**, *3*, 710.
(27) Qiu, H.; Cambridge, G.; Winnik, M. A.; Manners, I. Multi-Armed Micelles and Block Co-micelles via Crystallization-Driven Self-Assembly with Homopolymer Nanocrystals as Initiators. *J. Am. Chem. Soc.* **2013**, *135*, 12180−12183.
(28) Finnegan, J. R.; Lunn, D. J.; Gould, O. E. C.; Hudson, Z. M.; Whittell, G. R.; Winnik, M. A.; Manners, I. Gradient Crystallization-Driven Self-Assembly: Cylindrical Micelles with "Patchy" Segmented Coronas via the Coassembly of Linear and Brush Block Copolymers. *J. Am. Chem. Soc.* **2014**, *136*, 13835−13844.
(29) Hudson, Z. M.; Boott, C. E.; Robinson, M. E.; Rupar, P. A.; Winnik, M. A.; Manners, I. Tailored Hierarchical Micelle Architectures using Living Crystallization-Driven Self-Assembly in Two Dimensions. *Nat. Chem.* **2014**, *6*, 893−898.
(30) Jia, L.; Zhao, G.; Shi, W.; Coombs, N.; Gourevich, I.; Walker, G. C.; Guerin, G.; Manners, I.; Winnik, M. A. A Design Strategy for the Hierarchical Fabrication of Colloidal Hybrid Mesostructures. *Nat. Commun.* **2014**, *5*, 3882.
(31) Qian, J.; Li, X.; Lunn, D. J.; Gwyther, J.; Hudson, Z. M.; Kynaston, E.; Rupar, P. A.; Winnik, M. A.; Manners, I. Uniform, High Aspect Ratio Fiber-like Micelles and Block Co-micelles with a Crystalline π-Conjugated Polythiophene Core by Self-Seeding. *J. Am. Chem. Soc.* **2014**, *136*, 4121−4124.
(32) Gao, Y.; Qiu, H.; Zhou, H.; Li, X.; Harniman, R.; Winnik, M. A.; Manners, I. Crystallization-Driven Solution Self-Assembly of Block Copolymers with a Photocleavable Junction. *J. Am. Chem. Soc.* **2015**, *137*, 2203−2206.
(33) Qiu, H.; Gao, Y.; Du, V. A.; Harniman, R.; Winnik, M. A.; Manners, I. Branched Micelles by Living Crystallization-Driven Block Copolymer Self-Assembly under Kinetic Control. *J. Am. Chem. Soc.* **2015**, *137*, 2375−2385.
(34) Lazzari, M.; Scalarone, D.; Hoppe, C. E.; Vazquez-Vazquez, C.; Lòpez-Quintela, M. A. Tunable Polyacrylonitrile-Based Micellar Aggregates as a Potential Tool for the Fabrication of Carbon Nanofibers. *Chem. Mater.* **2007**, *19*, 5818−5820.
(35) Schmelz, J.; Karg, M.; Hellweg, T.; Schmalz, H. General Pathway toward Crystalline-Core Micelles with Tunable Morphology and Corona Segregation. *ACS Nano* **2011**, *5*, 9523−9534.
(36) Mihut, A. M.; Crassous, J. J.; Schmalz, H.; Drechsler, M.; Ballauff, M. Self-Assembly of Crystalline-Coil Diblock Copolymers in Solution: Experimental Phase Map. *Soft Matter* **2012**, *8*, 3163−3173.
(37) McGrath, N.; Schacher, F. H.; Qiu, H.; Mann, S.; Winnik, M. A.; Manners, I. Synthesis and Crystallization-Driven Solution Self-Assembly of Polyferrocenylsilane Diblock Copolymers with Polymethacrylate Corona-Forming Blocks. *Polym. Chem.* **2014**, *5*, 1923−1929.

DOI: 10.1021/acsami.5b05177
ACS Appl. Mater. Interfaces 2015, 7, 18697−18706

(38) He, W.-N.; Zhou, B.; Xu, J.-T.; Du, B.-Y.; Fan, Z.-Q. Two Growth Modes of Semicrystalline Cylindrical Poly(ε-caprolactone)-b-poly(ethylene oxide) Micelles. *Macromolecules* **2012**, *45*, 9768−9778.
(39) Sun, L.; Petzetakis, N.; Pitto-Barry, A.; Schiller, T. L.; Kirby, N.; Keddie, D. J.; Boyd, B. J.; O'Reilly, R. K.; Dove, A. P. Tuning the Size of Cylindrical Micelles from Poly(l-lactide)-b-poly(acrylic acid) Diblock Copolymers Based on Crystallization-Driven Self-Assembly. *Macromolecules* **2013**, *46*, 9074−9082.
(40) Yu, B.; Jiang, X.; Yin, J. Size-Tunable Nanosheets by the Crystallization-Driven 2D Self-Assembly of Hyperbranched Poly(ether amine) (hPEA). *Macromolecules* **2014**, *47*, 4761−4768.
(41) Zhang, W.; Müller, A. H. E. Architecture, Self-Assembly and Properties of Well-Defined Hybrid Polymers Based on Polyhedral Oligomeric Silsequioxane (POSS). *Prog. Polym. Sci.* **2013**, *38*, 1121−1162.
(42) Hirai, T.; Leolukman, M.; Jin, S.; Goseki, R.; Ishida, Y.; Kakimoto, M.-a.; Hayakawa, T.; Ree, M.; Gopalan, P. Hierarchical Self-Assembled Structures from POSS-Containing Block Copolymers Synthesized by Living Anionic Polymerization. *Macromolecules* **2009**, *42*, 8835−8843.
(43) Raftopoulos, K. N.; Koutsoumpis, S.; Jancia, M.; Lewicki, J. P.; Kyriakos, K.; Mason, H. E.; Harley, S. J.; Hebda, E.; Papadakis, C. M.; Pielichowski, K.; Pissis, P. Reduced Phase Separation and Slowing of Dynamics in Polyurethanes with Three-Dimensional POSS-Based Cross-Linking Moieties. *Macromolecules* **2015**, *48*, 1429−1441.
(44) Peng, J.; Xing, Y.; Xu, K.; Lin, W.; Wu, J.; Yu, Z.; Zhang, Y.; Chen, M. Fabrication of Silsesquioxane-Based Nano-Wrinkled Structures by Coupling the Polymeric Surface onto Rigid Templates Assembled from Unique Deca-Silsesquioxane. *J. Mater. Chem. C* **2015**, *3*, 2897−2908.
(45) Liu, F.; Zhang, Y.; Xu, L.; Zhang, W. Morphology-Controlled Self-Assembly of an Organic/Inorganic Hybrid Porphyrin Derivative Containing Polyhedral Oligomeric Silsesquioxane (POSS). *Chem. - Eur. J.* **2015**, *21*, 5540−5547.
(46) Li, D.; Niu, Y.; Yang, Y.; Wang, X.; Yang, F.; Shen, H.; Wu, D. Synthesis and Self-Assembly Behavior of POSS-embedded Hyperbranched Polymers. *Chem. Commun.* **2015**, *51*, 8296−8299.
(47) Liao, W.-H.; Yang, S.-Y.; Hsiao, S.-T.; Wang, Y.-S.; Li, S.-M.; Ma, C.-C. M.; Tien, H.-W.; Zeng, S.-J. Effect of Octa(aminophenyl) Polyhedral Oligomeric Silsesquioxane Functionalized Graphene Oxide on the Mechanical and Dielectric Properties of Polyimide Composites. *ACS Appl. Mater. Interfaces* **2014**, *6*, 15802−15812.
(48) Li, Z.; Wu, D.; Liang, Y.; Fu, R.; Matyjaszewski, K. Synthesis of Well-Defined Microporous Carbons by Molecular-Scale Templating with Polyhedral Oligomeric Silsesquioxane Moieties. *J. Am. Chem. Soc.* **2014**, *136*, 4805−4808.
(49) Li, J.; Zhou, Z.; Ma, L.; Chen, G.; Li, Q. Hierarchical Assembly of Amphiphilic POSS-Cyclodextrin Molecules and Azobenzene End-Capped Polymers. *Macromolecules* **2014**, *47*, 5739−5748.
(50) Hou, H.; Gan, Y.; Yin, J.; Jiang, X. Multifunctional POSS-Based Nano-Photo-Initiator for Overcoming the Oxygen Inhibition of Photo-Polymerization and for Creating Self-Wrinkled Patterns. *Adv. Mater. Interfaces* **2014**, *1*, 1400385.
(51) Gan, Y.; Jiang, X.; Yin, J. Self-Wrinkling Patterned Surface of Photocuring Coating Induced by the Fluorinated POSS Containing Thiol Groups (F-POSS-SH) as the Reactive Nanoadditive. *Macromolecules* **2012**, *45*, 7520−7526.
(52) Watanabe, A.; Qin, G.; Cheng, C.-W.; Shen, W.-C.; Chu, C.-I. Hydrophobic Surface Based on Microtexture of Ag Nanoparticle/POSS Nanocomposite Film. *Chem. Lett.* **2013**, *42*, 1255−1256.
(53) Feng, Y.; Jia, Y.; Guang, S.; Xu, H. Study on Thermal Enhancement Mechanism of POSS-containing Hybrid Nanocomposites and Relationship between Thermal Properties and Their Molecular Structure. *J. Appl. Polym. Sci.* **2010**, *115*, 2212−2220.
(54) Lu, C.-H.; Kuo, S.-W.; Huang, C.-F.; Chang, F.-C. Self-Assembled Fernlike Microstructures of Polyhedral Oligomeric Silsesquioxane/Gold Nanoparticle Hybrids. *J. Phys. Chem. C* **2009**, *113*, 3517−3524.
(55) Xu, G.; Tazawa, M.; Jin, P.; Nakao, S.; Yoshimura, K. Wavelength Tuning of Surface Plasmon Resonance Using Dielectric Layers on Silver Island Films. *Appl. Phys. Lett.* **2003**, *82*, 3811−3813.
(56) Taleb, A.; Petit, C.; Pileni, M. P. Optical Properties of Self-Assembled 2D and 3D Superlattices of Silver Nanoparticles. *J. Phys. Chem. B* **1998**, *102*, 2214−2220.
(57) Wang, Y.; Chen, H.; Dong, S.; Wang, E. Surface-Enhanced Raman Scattering of Silver-Gold Bimetallic Nanostructures with Hollow Interiors. *J. Chem. Phys.* **2006**, *125*, 044710.
(58) Zhou, Q.; Zhao, G.; Chao, Y.; Li, Y.; Wu, Y.; Zheng, J. Charge-Transfer Induced Surface-Enhanced Raman Scattering in Silver Nanoparticle Assemblies. *J. Phys. Chem. C* **2007**, *111*, 1951−1954.
(59) Osawa, M.; Matsuda, N.; Yoshii, K.; Uchida, I. Charge Transfer Resonance Raman Process in Surface-Enhanced Raman Scattering from *p*-Aminothiophenol Adsorbed on Silver: Herzberg−Teller Contribution. *J. Phys. Chem.* **1994**, *98*, 12702−12707.

DOI: 10.1021/acsami.5b05177
ACS Appl. Mater. Interfaces 2015, 7, 18697−18706